An Experimental–Computational Study of Catheter Induced Alterations in Pulse Wave Velocity in Anesthetized Mice

Federica Cuomo, Jacopo Ferruzzi, Jay D. Humphrey & C. Alberto Figueroa

Annals of Biomedical Engineering
The Journal of the Biomedical
Engineering Society

ISSN 0090-6964
Volume 43
Number 7

Ann Biomed Eng (2015) 43:1555-1570
DOI 10.1007/s10439-015-1272-0

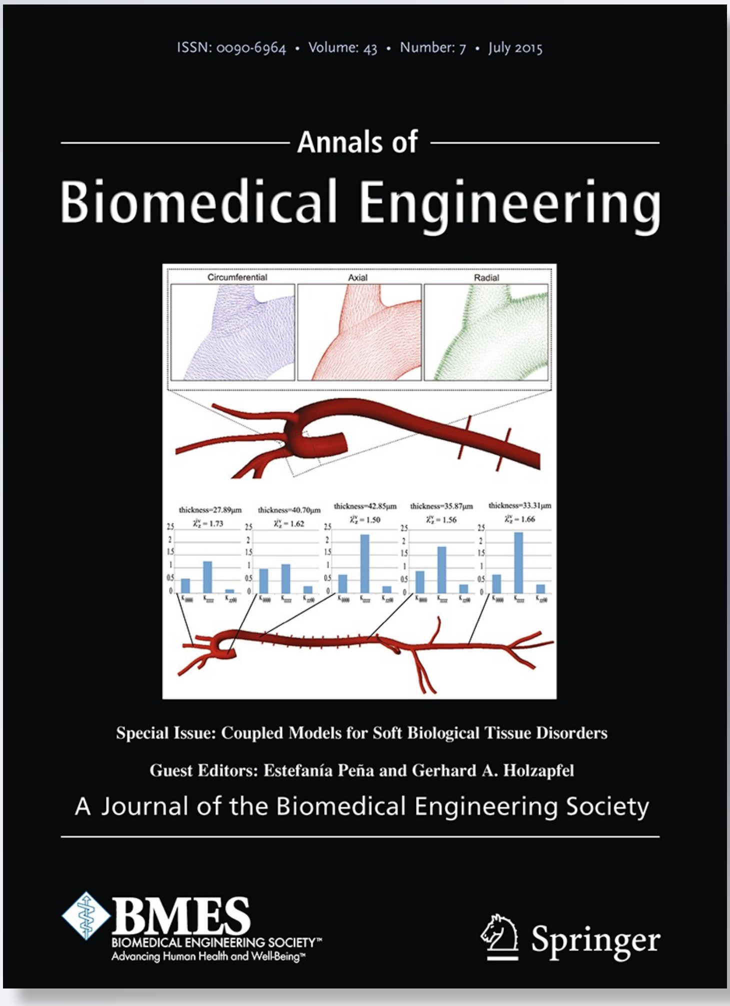

Springer

Annals of Biomedical Engineering, Vol. 43, No. 7, July 2015 (*© 2015*) pp. 1555–1570
DOI: 10.1007/s10439-015-1272-0

An Experimental–Computational Study of Catheter Induced Alterations in Pulse Wave Velocity in Anesthetized Mice

FEDERICA CUOMO,[1,4] JACOPO FERRUZZI,[2] JAY D. HUMPHREY,[2] and C. ALBERTO FIGUEROA[1,3,4]

[1]Department of Biomedical Engineering, King's College London, London, UK; [2]Department of Biomedical Engineering, Yale University, New Haven, CT, USA; [3]Department of Surgery, University of Michigan, Ann Arbor, MI, USA; and [4]Department of Biomedical Engineering, University of Michigan, Ann Arbor, MI, USA

(Received 12 August 2014; accepted 1 February 2015; published online 20 February 2015)

Associate Editor Estefanía Peña oversaw the review of this article.

Abstract—Computational methods for solving problems of fluid dynamics and fluid–solid-interactions have advanced to the point that they enable reliable estimates of many hemodynamic quantities, including those important for studying vascular mechanobiology or designing medical devices. In this paper, we use a customized version of the open source code *SimVascular* to develop a computational model of central artery hemodynamics in anesthetized mice that is informed with experimental data on regional geometries, blood flows and pressures, and biaxial wall properties. After validating a baseline model against available data, we then use the model to investigate the effects of commercially available catheters on the very parameters that they are designed to measure, namely, murine blood pressure and (pressure) pulse wave velocity (PWV). We found that a combination of two small profile catheters designed to measure pressure simultaneously in the ascending aorta and femoral artery increased the PWV due to an overall increase in pressure within the arterial system. Conversely, a larger profile dual-sensor pressure catheter inserted through a carotid artery into the descending thoracic aorta decreased the PWV due to an overall decrease in pressure. In both cases, similar reductions in cardiac output were observed due to increased peripheral vascular resistance. As might be expected, therefore, invasive transducers can alter the very quantities that are designed to measure, yet advanced computational models offer a unique method to evaluate or augment such measurements.

Keywords—Mouse hemodynamics, Aortic stiffness, Central pulse pressure, Fluid–solid-interaction.

INTRODUCTION

Since the mid-1990s, genetically modified mice have been used widely to study cardiovascular diseases and their treatment. With this increased use of mice came a need for new methods and devices for data acquisition. Many of the requisite measurements are complicated, however, by the smallness of the cardiovascular system and high heart rate in mice; non-invasive and invasive methods of measurement thus remain in continual development. Furthermore, given the difficulty of performing studies on conscious mice, anesthesia is often required for both non-invasive and invasive measurements. Since anesthesia alters heart rate, cardiac output, and blood pressure, these changes must be considered when interpreting data on cardiovascular function. Among the many available anesthetic agents, 1–2% isoflurane delivered by inhalation has been proven to preserve cardiovascular function better than others, with physiologic and hemodynamic parameters closer to those measured under conscious conditions.[16]

Like anesthesia, many invasive methods of measuring cardiovascular parameters also alter the very quantity that is of interest. Prime examples include measurement of central (blood) pulse pressure (cPP), and the (pressure) pulse wave velocity (PWV), each of which is typically achieved by introducing a catheter within the vasculature or cardiac chamber either acutely or chronically (as needed for telemetry systems). The potential impact of a pressure catheter on the hemodynamics of the mouse remains unclear from a theoretical perspective and necessarily cannot be evaluated experimentally without invoking many assumptions. There is a pressing need, therefore, to understand better the effects of measurement technique on the data collected and, accordingly, to identify the best methods to

---

Address correspondence to C. Alberto Figueroa, Department of Biomedical Engineering, University of Michigan, Ann Arbor, MI, USA. Electronic mail: figueroc@med.umich.edu

Federica Cuomo and Jacopo Ferruzzi have contributed equally.

assess cPP or PWV. Toward this end, computational modeling offers an objective, nonintrusive approach for evaluating current methods of measurement as well as for identifying possible improvements in experimental design or even new technological approaches to measure hemodynamics in mice.

In this paper, we use a customized version of the well validated fluid-solid-interaction (FSI) code *SimVascular* to compare computational results for a baseline model of anesthetized mouse hemodynamics with experimental data. Following tuning and validation of the baseline model, we evaluate potential effects on the hemodynamics due to the use of two commercially available catheters for measuring cPP and aortic PWV. The latter metric necessarily requires simultaneous acquisition of two pressure or two flow waveforms at two locations along the vascular tree as well as knowledge of the distance between these locations. That is, PWV is typically evaluated as the distance between two measuring locations divided by a metric of the phase lag for the two recorded waveforms. The computational models considered in this paper reproduce two different approaches to simultaneously acquire pressure waveforms at two different locations. The overall computational model includes a heart model to capture ventricular-vascular coupling, which allows an evaluation of how cardiac output varies with different afterload conditions resulting from either anesthesia or insertion of a catheter.

METHODS

Biomechanical Experiments

All animal procedures were approved by the Institutional Animal Care and Use Committee of Yale University. Male wild-type mice on a mixed C57BL/6 × 129/SvEv background were used between 20 and 27 weeks of age. Specific experimental and theoretical methods for quantifying physiological variables and biomechanical properties are described in detail elsewhere.[5] Herein, we only review basic procedures and present those data fundamental for informing the present computational model. All *in vivo* data were acquired under isoflurane anesthesia since we sought to capture the hemodynamics under typical experimental conditions. By altering heart rate and cardiac output, anesthesia reduces blood pressure and thus both the vascular geometry (inner radius and wall thickness) and wall stiffness that are important determinants of cPP and PWV.

Geometry

The basic computational domain was obtained *via* vascular corrosion casting. Briefly, a single mouse was euthanized at 27 weeks of age *via* an overdose of Beuthanasia, the thoracic cavity was opened surgically, and the left ventricle was cannulated at its apex using a 21G needle. The aorta was then flushed with heparinized saline (110 U kg^{-1}) and perfusion fixed at 100 mmHg for 1 h with 10% formalin. The superior vena cava was used as an exit site during flushing, but was subsequently closed using 6-O sutures to enable pressurization. A Batson's no. 17 Plastic Replica Kit (Polysciences, Warrington, PA) was used to fill the aorta and major branches with plastic while maintaining a perfusion pressure of ~100 mmHg within the ventricle. The mouse was subsequently immersed overnight in an ice bath to allow heat to dissipate while the polymer cured and the body was macerated in 25% KOH. The resulting plastic cast (Fig. 1a) was digitized using micro-CT (eXplore CT120, GE Healthcare). The image stack had a spatial resolution of 49.217 × 49.217 × 98.434 microns with dimensions of 480 × 328 × 858 voxels. Arterial cross-sections were segmented semi-automatically using a 2D level set method within a customized version of the open source software package *SimVascular* (SimBios National Center for Biomedical Computing, Stanford, CA), thus yielding a 3D geometric model of the mouse aorta and its major branches (Fig. 1b).

Physiological Measurements

We used illustrative non-invasive and invasive data collected from another mouse (20 weeks of age) to inform our baseline computational model since the vascular corrosion casting is a destructive technique. Briefly, the mouse was anesthetized using 1.5% isoflurane and secured on a heated surgical platform (Indus Instruments, Houston, TX) to monitor cardiac and respiratory rates. Ultrasound data were collected using a Vevo 2100 system (Visualsonic, Toronto, Canada). B-mode imaging was used to locate the ascending thoracic aorta (ATA), proximal descending thoracic aorta (DTA), suprarenal abdominal aorta (SAA), infrarenal abdominal aorta (IAA), and one common carotid artery (CCA). For each of these sections, M-mode sequences were recorded for a short axis view and used to measure inner diameters at systole and diastole from nine cardiac cycles. Average diameters for the different sections are shown in Table 1. Color Doppler imaging was used to find the long axis view that would allow the most accurate measurements of mean blood velocity in both the ATA and IAA. Pulsed Doppler data were thus collected just after the aortic valve in the ATA and just before the iliac bifurcation in the IAA; all measurements were angle corrected. Similar to Trachet *et al.*,[30] we employed the auto-trace function within the Vevo 2100

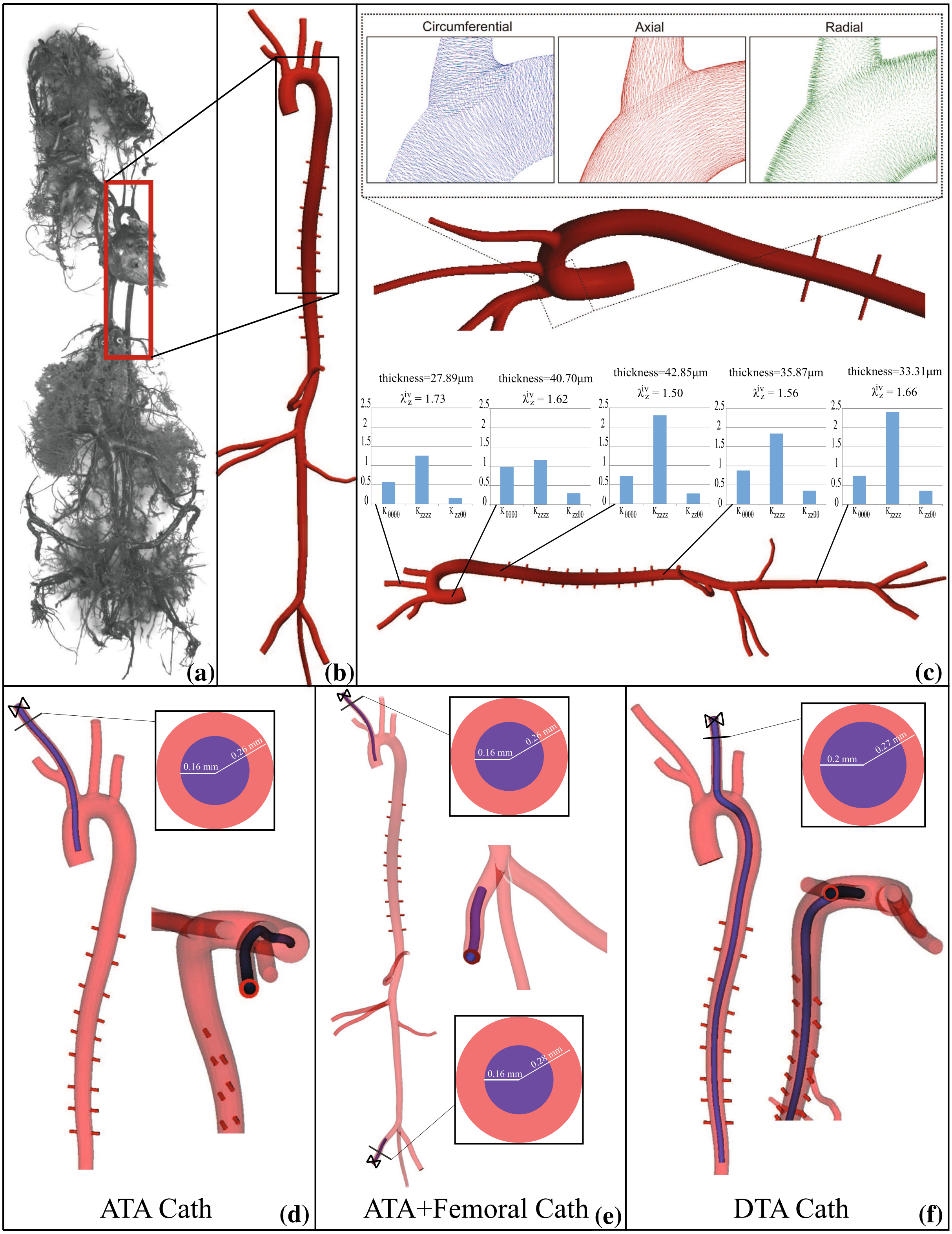

FIGURE 1. (a) Corrosion cast of the vasculature in an illustrative example of adult mouse; (b) Computational model of the aorta and main branches built from the cast; (c) Regional biaxial tissue properties in the ATA, DTA, SAA, IAA, and CCA locations, mapped to the mouse-specific geometry; (d) ATA Cath model; (e) ATA + Femoral Cath model; (f) DTA Cath model.

TABLE 1. ***In vivo* internal diameters.**

ATA		DTA		SAA		IAA		CCA	
Systole (mm)	Diastole (mm)	Systole (mm)	Diastole (mm)	Systole (mm)	Diastole (mm)	Systole (mm)	Diastole (mm)	Systole (mm)	Diastole (mm)
1.563	1.193	1.361	1.153	1.129	0.868	0.782	0.678	0.606	0.502

Listed are the *in vivo* internal diameters at peak systole and diastole for the five primary arterial segments in the vascular model: ascending thoracic aorta (*ATA*), descending thoracic aorta (*DTA*), suprarenal abdominal aorta (*SAA*), infra-renal abdominal aorta (*IAA*), common carotid artery (*CCA*), as measured by M-mode ultrasound.

data analysis software to extract blood velocity waveforms over multiple cardiac cycles. Raw data were analyzed using MATLAB (Mathworks, Natick, MA), including outlier elimination and ensemble averaging to obtain an average waveform representing a mean cardiac cycle. Similar to Gaddum *et al.*,[9] we defined the foot of the blood velocity waveform as the intersection between two tangents: the horizontal tangent intersecting its diastolic minimum and the tangent to the maximum systolic gradient, which was evaluated using a 4th-order accurate central differences scheme (given the constant sampling rate). Hence, the aortic pulse transit time was calculated as the time lag between the average feet of the ATA and IAA blood velocities. Finally, a SPR-1000 pressure catheter (Millar, Houston, TX) having a 1F outer diameter tip was inserted *via* the right common carotid artery and positioned halfway between the aortic root and the base of the brachiocephalic artery. Correct positioning of the pressure transducer was assessed *via* B-Mode ultrasound imaging and continuous pressure data were recorded over multiple cardiac cycles. Central blood pressures measured under isoflurane anesthesia revealed systolic and diastolic values of 96 and 65 mmHg, respectively. Aortic pressure waveforms were ensemble averaged using the R-peak of the EKG signal to separate adjacent cardiac cycles. The resulting mean ATA pressure waveform was used to inform and to validate our computational model.

Biaxial Arterial Properties

Mean biaxial data sets ($n = 5$ mice, 21.3 ± 0.4 weeks of age) for each of the aforementioned five primary measurement sites (ATA, DTA, SAA, IAA, and CCA) consisted of pressure–diameter (*P–d*) protocols performed separately at three fixed axial stretches (*in vivo* and 5% above and below *in vivo*) and axial force–length (*f–l*) protocols performed separately at four fixed pressures (10, 60, 100, and 140 mmHg). These protocols are designed to characterize the behavior of arterial tissue exposed not only to the luminal pressure, but also to a considerable degree of axial stretching. Experimental pressure, diameter, axial force, and axial stretch data from these seven protocols were reduced using a two-dimensional four-fiber family constitutive model[6] to fit the observed behaviors. Using the theory of small deformations superimposed on large,[1] the nonlinear material behavior was linearized to obtain *in vivo* relevant values of anisotropic wall stiffness using the individual *in vivo* value of axial stretch for each region and the mean blood pressure measured invasively under anesthesia (i.e., 75 mmHg). Our FSI formulation (see Sect. 2.2) employs an enhanced linearized membrane model of the wall, whereby the non-zero values of the stiffness tensor are organized within a 5×5 matrix for each site.[7] The order of the components of this stiffness matrix corresponds to the directions: $\theta\theta$, ZZ, θZ, $\rho\theta$, and ρZ; where θ is the circumferential direction, Z the axial direction and ρ the radial direction. This stiffness matrix is first defined in the cylindrical coordinates of the mechanical testing, but then transformed according to the local *in vivo* coordinate system given by unit normal vectors in circumferential, axial, and radial directions (see Fig. 1c).

Simulation Framework

We employed a multi-scale, multi-domain modeling approach that combines a heart model, a 3D geometrical vascular model, a FSI model to account for the deformability of the central vessels, and Windkessel models to represent the distal vascular beds. Our strategy was, first, to define a baseline computational model for a mouse that reproduced the measured anesthetized conditions and, second, to investigate how PWV is altered by invasive measurements, namely, when assessed using two different commercially available catheter systems.

Geometry

Micro-CT measurements of the vascular cast were reconstructed using a customized version of *SimVascular* to obtain a basic geometric model. The primary segments constituting the model were the aorta (including the ATA, DTA, SAA, and IAA) as well as the subclavian, carotid, renal, mesenteric, celiac, and tail arteries. Despite multiple attempts, the corrosion casting process (euthanized conditions) did not maintain the precise dimensions measured non-invasively (anesthetized conditions), hence diameters reconstructed from the micro-CT data were scaled using *in vivo* data measured with M-mode ultrasound (Table 1). Specifically, the centroid and radius were first determined along each vascular segment, then the inner radii were scaled up (or down) such that the mean radius of each segment matched the expected dimension. Different scaling factors were used for each segment; for those vessels for which a known diameter was not available, the scale factor of the closest segment was used. Our casting method did not provide confident visualization of the intercostal arteries, which account for a significant percentage of the cardiac output due to the large size of the mouse rib cage relative to the rest of the body. To render both the pressure gradient along the thoracic aorta and the relevant flow distributions more realistic, intercostal arteries were added using reported reference diameters and branch distances (Table 2).[11] For each of the nine pairs of intercostals, branch locations were defined as relative lengths along the aorta, namely the path spline. Branch origins were defined using the mean of the centers of the two nearest aortic segments, weighted by the relative distance to each segment. The intercostal paths were defined as straight lines parallel to the branching angle of the corresponding renal artery and perpendicular to the aorta path.

After building the baseline model (Fig. 1b), two additional 3D models were created to represent illustrative scenarios whereby commercial catheters are used to assess PWV.[17,33] In the first scenario, two 1F diameter catheters (SPR-1000; Millar, Houston, TX) are inserted and secured in the ATA (*via* the right CCA) and in the right iliac artery (*via* the right femoral artery). Herein, we refer to this model as the ATA + Femoral Cath (Fig. 1e). In the second scenario, a 1.2F diameter dual-sensor pressure catheter (Scisense, Inc., London, Ontario, Canada) is inserted through the left CCA down into the descending aorta, covering a much longer length in part due to the need to host two pressure sensors. We refer to this model as the DTA Cath (Fig. 1f). For the sake of completeness, we considered a third scenario in which a single Millar catheter is inserted in the right CCA and into the ATA or left ventricle. This scenario, used experimentally to quantify pressure in the ascending aorta or left ventricle, does not enable the assessment of PWV as it does not provide simultaneous recordings of pressure at two different locations. We refer to this model as ATA Cath (Fig. 1d) and we considered it in order to reproduce the hemodynamic conditions during our experimental measurements. We assumed that the catheters were stiff and fixed in position throughout the cardiac cycle without contacting any of the vessel boundaries. Furthermore, given that the blood vessel around the catheter is usually occluded with a ligature to prevent bleeding, we enforced complete occlusion in the vessels where the catheters are inserted and secured.

TABLE 2. Fractional longitudinal position of the intercostal pairs along the aorta.[11]

Location down the aorta	Fractional longitudinal position
Aortic semilunar valve	0
First pair of intercostal arteries	0.20 ± 0.013
Second pair of intercostal arteries	0.24 ± 0.014
Third pair of intercostal arteries	0.29 ± 0.0066
Fourth pair of intercostal arteries	0.34 ± 0.0087
Fifth pair of intercostal arteries	0.38 ± 0.0080
Sixth pair of intercostal arteries	0.42 ± 0.0064
Seventh pair of intercostal arteries	0.47 ± 0.0087
Eight pair of intercostal arteries	0.51 ± 0.0096
Ninth pair of intercostal arteries	0.55 ± 0.012
Common iliac artery	1

Mesh Adaptation

Initial meshes of linear tetrahedral elements were generated using meshing libraries in *SimVascular*. A global value for an element size of 0.08 mm was used together with a local refinement in the intercostal arteries. Within these parameters, a mesh of 1.2 million elements and 250 thousand nodes was obtained for the baseline model; 1.9 million elements and 400 thousand nodes for the ATA Cath; 2.1 million elements and 433 thousand nodes for the ATA + Femoral Cath; and 3.1 million elements and 623 thousand nodes for the DTA Cath. These initial meshes were used to run simulations for seven cardiac cycles using 2700 time steps per cycle ($T_{\text{cycle}} = 0.135$s). The results of these simulations were then used to adapt the meshes based on the distributions of velocity gradients (Hessians) throughout the arterial network. The mesh adaptation algorithm reduced or increased the mesh density in regions of low or high velocity gradients, respectively.[26] Finally, mesh independence studies were performed to obtain converged values of PWV in the final meshes; for this purpose we adopted a two-step mesh adaptation strategy. The final adapted meshes had 1.4 million elements and 273 thousand nodes for the baseline, 1.3 million and 259 thousand nodes for the ATA Cath, 3.0 million and 557 thousand nodes for the ATA + Femoral Cath, and 1.6 million elements and 315 thousand nodes for the DTA Cath models.

Computational Methods

Similar to our prior large-scale study of the human arterial tree,[36] we used a multi-domain framework to study the hemodynamics in the four different models. Namely, we modeled pressure and velocity fields in all vessels from the heart to the capillaries using a Dirichlet-to-Neuman variational FSI multi-scale method. In particular, we coupled a novel lumped parameter heart model with the inlet surface of the 3D model and we coupled more traditional lumped parameter Windkessel models with the outlet surfaces throughout the arterial tree.

The heart model consisted of a series of 0D components representing chambers and valves; the pumping action of the heart, modeled using a time-varying elastance, generated flow and pressure within the coupled 3D model. Details on the heart model can be found elsewhere.[18,19,29] Parameters for the heart model (Table 3) were tuned to obtain a cardiac output of 12 mL min^{-1} consistent with reports by others[4] as well as experimentally measured pressures for the baseline model (96 mmHg systolic, 65 mmHg diastolic). Thereafter, the parameters were kept fixed for the three different catheters geometries, with the assumption that the heart has a decreased ability to adapt to different afterload conditions under anesthesia.[28,31] The Windkessel models coupled to each outlet of the 3D domain represent effects from small arteries and arterioles down to the capillary level; for details, see Vignon-Clementel *et al.*[32] Specific values of the parameters of the Windkessel models were computed using a 1D theory,[35] then tuned to reach reported values flow splits[4,10,14] (Table 6) and pressures measured *in vivo*. The tuned parameters (Table 4) were used for all four simulations, hypothesizing that effects on vasodilatation or vasoconstriction due to anesthesia did not change with the placement of different catheters.

TABLE 3. Heart model parameters.

Maximum elastance [Pa (mm^3)$^{-1}$]	430
Time to maximum elastance (s)	0.07
Time to relax (s)	0.0125
End diastolic volume (mm^3)	44
Atrial preload (Pa)	667
Aortic valve	
Resistance [Pa s (mm^3)$^{-1}$]	0.0001
Inductance [Pa s (mm^3)$^{-1}$]	0.0001
Mitral valve	
Resistance [Pa s (mm^3)$^{-1}$]	0.0001
Inductance [Pa s (mm^3)$^{-1}$]	0.0001
Left ventricular resistance [Pa s (mm^3)$^{-1}$]	0.00015

Heart model parameters tuned to match desired levels of cardiac output given in the literature, and the experimentally measured pressure for the baseline model.

TABLE 4. Tuned Windkessel parameters.

Vascular segment	R_p [Pa s (mm^3)$^{-1}$]	C [Pa (mm^3)$^{-1}$]	R_d [Pa s (mm^3)$^{-1}$]
Right common carotid	38.10	2.81×10^{-4}	560.31
Left common carotid	44.71	3.23×10^{-4}	488.08
Right subclavian	40.29	2.69×10^{-4}	585.44
Left subclavian	23.52	3.54×10^{-4}	443.21
Intercostal	189.74	4.48×10^{-5}	3512.80
Celiac	61.38	1.76×10^{-4}	892.23
Mesenteric	68.24	1.62×10^{-4}	969.62
Right renal	52.23	2.00×10^{-4}	785.85
Left renal	134.53	9.55×10^{-5}	1651.87
Right iliac	31.26	2.31×10^{-4}	680.06
Left iliac	2.19	2.25×10^{-4}	696.05
Tail	11.17	8.55×10^{-5}	851.70

Tuned Windkessel parameters: R_p, C, R_d represent, respectively, the proximal resistance, the compliance and the distal resistance for each outlet.

Blood flow–vessel wall interactions are fundamental to capture wave propagation within an arterial network; they were modeled herein using a coupled-momentum method.[8] The wall properties were prescribed in three steps. First, the regionally dependent values of linearized anisotropic tissue stiffness that were measured *in vitro* (ATA, DTA, SAA, IAA, and CCA) were mapped directly onto segments corresponding to the excised vessels (Fig. 1c). Second, values of stiffness within regions bounded proximally and distally by measured values were populated by linearly interpolating the local values. Third, by assuming little variation in properties under anesthesia, distal values of stiffness were prescribed based on data taken from the closest location: the stiffness of the iliac and the tail arteries ware prescribed from the IAA, that for middle branches (right and left renal, celiac, mesenteric arteries) were set with values from the nearest point in the abdominal aorta, and that for upper branches (right and left carotids and subclavians) were set to have the stiffness of the common carotid.

To capture the nonlinear behavior, whereby higher stiffness is observed for higher stresses, an iterative approach adjusted the values of stiffness in response to any changes in pressure that resulted from introducing a catheter. Specifically, the linearized stiffness computed from the four-family constitutive model was initially calculated using a mean pressure of 75 mmHg along the entire model, corresponding to the mean aortic pressure measured in the ascending aorta *in vivo*. After running a simulation, the distribution of mean pressures along the model was used to recalculate regional values of linearized stiffness and the simulation was run again with the updated values. This process was adopted for each of the four cases. The iterative procedure was terminated when the current mean pressures differed from the mean pressures from the previous iteration by less than 2% (Table 5).

Lastly, another important aspect in a FSI simulation is the load exerted by perivascular tissue and other organs on the arterial wall. Among other effects, perivascular support helps to prevent non-physio-

TABLE 5. Linearized stiffness and thickness values.

	ATA	DTA	SAA	IAA	CAA
Baseline					
$C_{\theta\theta}$ (MPa)	0.98	0.72	0.88	0.75	0.57
C_{ZZ} (MPa)	1.16	2.29	1.80	2.32	1.23
h (μm)	40.69	42.93	36.07	33.61	27.98
ATA Cath					
$C_{\theta\theta}$ (MPa)	1.05	0.76	0.90	0.73	0.60
C_{ZZ} (MPa)	1.19	2.37	1.86	2.39	1.29
h (μm)	40.31	42.59	35.77	33.40	27.77
ATA + Femoral Cath					
$C_{\theta\theta}$ (MPa)	1.09	0.80	0.96	0.78	0.64
C_{ZZ} (MPa)	1.20	2.43	1.92	2.48	1.34
h (μm)	40.06	42.31	35.49	33.13	27.61
DTA Cath					
$C_{\theta\theta}$ (MPa)	1.02	0.73	0.76	0.64	0.58
C_{ZZ} (MPa)	1.18	2.32	1.72	2.23	1.27
h (μm)	40.43	42.79	36.5	33.92	27.85

Tuned linearized stiffness and thickness for each case at five different locations: ascending thoracic aorta (*ATA*), descending thoracic aorta (*DTA*), supra-renal abdominal aorta (*SAA*), infra-renal abdominal aorta (*IAA*) and common carotid artery (*CAA*). $C_{\theta\theta}$ and C_{ZZ} refer respectively to the circumferential and axial component of the 5 × 5 stiffness matrix; h is the vessel wall thickness.

logical oscillations in the computed wall motion. A simple traction boundary condition was applied on the outer boundary of each vascular segment in the 3D model to represent the mechanical behavior of the perivascular tissue; details can be found in Moireau *et al.*[24] This traction boundary condition consisted of a viscoelastic term with two parameters that can be adjusted to mimic the response of various physiological tissues: k_s is a stiffness coefficient (assumed to be 10 Pa) and c_s is a damping coefficient (assumed to be 10 Pa s m^{-1}). The complete weak form of the variational multi-scale FSI formulation of the blood flow problem solved with this approach is thus:

$$\begin{aligned}&\int_{\Omega}\{\boldsymbol{w}\cdot(\rho\dot{\boldsymbol{v}}+\rho\boldsymbol{v}\cdot\nabla\boldsymbol{v}-\boldsymbol{f})+\nabla\boldsymbol{w}:(-p\boldsymbol{I}+\boldsymbol{\tau})-\nabla q\cdot\boldsymbol{v}\}dv\\&+\int_{\Gamma_{h1}}(q\boldsymbol{v}\cdot\boldsymbol{n}-\boldsymbol{w}\cdot\boldsymbol{t}^{h})da\;+\int_{\Gamma_{h2}}(q\boldsymbol{v}\cdot\boldsymbol{n}-\boldsymbol{w}\cdot\boldsymbol{t}^{h})da\\&+\int_{\Gamma_t}(q\boldsymbol{v}\cdot\boldsymbol{n})da+\int_{\Gamma_s}h\rho^{s}\boldsymbol{w}\cdot\dot{\boldsymbol{v}}dA\;+\int_{\Gamma_s}h\nabla\boldsymbol{w}:\mathcal{L}(\boldsymbol{P}\kappa_s)dA\\&-\int_{\Gamma_s}\boldsymbol{w}\cdot(k_s\boldsymbol{u}+c_s\boldsymbol{v})dA+\text{stabilization terms}=0\\&\forall\boldsymbol{x}(t)\in\bar{\Omega},\forall t\in[0,T].\end{aligned}$$

Here, Ω is the 3D domain, $\boldsymbol{v}$ is the blood velocity, and p the blood pressure; q and $\boldsymbol{w}$ are test functions for mass and momentum balance; ρ and ρ^s are the mass densities for the blood and wall, respectively; h is the wall thickness; Γ_{h1} is the inlet boundary coupled to the heart model; Γ_{h2} is the outlet boundary coupled to the Windkessel models; and Γ_s and Γ_t are the reference and current configurations of the arterial wall over the cardiac cycle, respectively. Finally, $\mathcal{L}(\boldsymbol{P}\kappa_s)$ is the linearization of the nonlinear constitutive relation for the arterial wall based on the small-on-large theory.[1]

RESULTS

Baseline Hemodynamics

Our baseline model reproduced well diverse data from both the literature and our experiments. Figure 2 shows simulated and measured central aortic pressures as well as pulse wave velocity, peak systolic pressures, wall shear stresses (WSS), a volume rendering of the magnitudes of velocity, and a series of flow waveforms at selected locations along the vasculature. The cardiac output produced by the heart model was tuned to 12.03 mL min^{-1}, consistent with values reported for the same strain of mice.[4,22] The central aortic pressure compared favorably with our *in vivo* invasive pressure measurements under anesthesia. Note that neither cardiac output nor ascending aortic pressure were imposed in the simulation; rather, they resulted from the choice of parameters in the heart and Windkessel models, which were adequately tuned to match the experimental data.

Values of PWV from the ascending aorta to the abdominal aorta just before the iliac bifurcation were calculated using an algorithm implemented in MATLAB[9] based on the transient time between two pressure waveforms recorded simultaneously at two different locations (Fig. 2, left bottom panel). The simulated transient time Δt was 10.8 ms, close to the experimentally measured time of 12.7 ms. Given that the distance between the two sites along the aortic centerline is 47.78 mm, a PWV of 4.42 m s^{-1} was obtained in the computations, which is similar to values reported in the literature (3.79 m s^{-1}) for the same strain of mouse[12] (noting that each mouse has a slightly different geometry and material properties, and each experiment has a different depth of anesthesia).

The computed distribution of flow also matched data in the literature. In particular, we compared our results with those of Feintuch *et al.* (Table 6) who measured flow in the innominate artery and left common carotid using MRI.[4] Their measurements were under 1.6% isoflurane anesthesia, similar to that used in our *in vivo* studies. We also compared our computed flow waveforms to those reported by Greve *et al.* for the infra-renal abdominal aorta in anesthetized mice[10] (Table 6). Lastly, as revealed by the left panel of

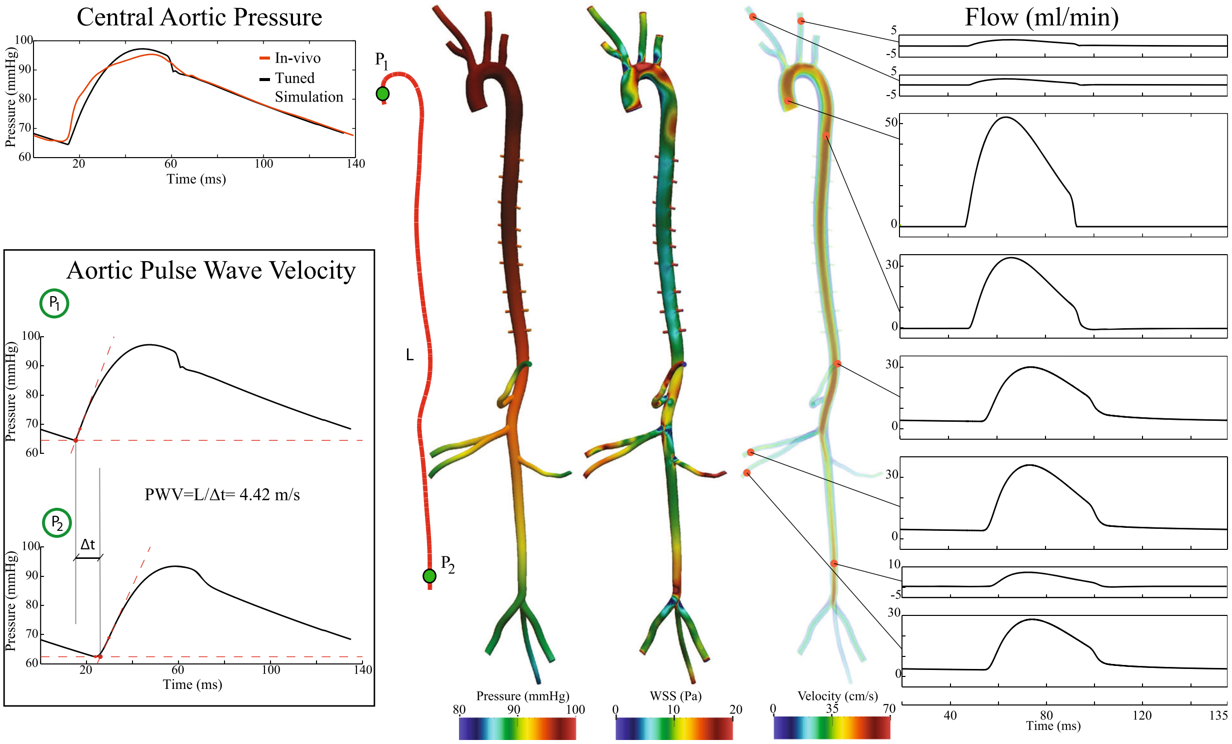

FIGURE 2. Computed hemodynamics for the baseline model. Comparison between *in vivo* and computed central aortic pressure: the heart model was tuned to reproduce the *in vivo* pressure (top left). Computed value of PWV based on pressure waves computed at two specific locations, P_1 and P_2 (bottom left). Center: Computed maps of blood pressure, wall shear stress, and blood velocity at peak systole. Right: Illustrative computed flow waveforms at multiple sites along the mouse arterial tree.

TABLE 6. Blood flow distribution.

Location	References	Technique	# of mice	% CO (data)	% CO (baseline simulation)
Innominate artery	Feintuch *et al.*[4]	MRI	5	16.9	17.4
Left carotid	Feintuch *et al.*[4]	MRI	5	10.4	10.0
Infra-renal abdominal aorta	Greve *et al.*[10]	MRI	5	17.5	16.6

Comparison of regional distributions of blood flow (given as cardiac output percentage) between the baseline simulation and values available in the literature for comparable conditions.

Fig. 2, the qualitative shapes of the computed flows agreed well with those previously reported in experiments by Hartley.[14] Overall, because we reproduced cardiac output, ascending aortic pressure, aortic-iliac PWV, flow distributions, and qualitative shapes of the flow waveforms, we were confident that the model captured well the baseline hemodynamics of a healthy mouse under anesthesia.

Comparison of Hemodynamics in Baseline and Catheter Models

It is well known that anesthesia relaxes vascular tone and baroreflex sensitivity, thus resulting in hypotension.[3] Diminished blood pressure is due, in part, to a decrease in both peripheral vascular resistance and cardiac output due to the anesthesia. In particular, isoflurane disrupts normal cardiovascular function by affecting the vasculature, myocardium, and sympathetic and parasympathetic branches of the autonomous nervous system.[27] In general, it is difficult to assess the extent to which different drugs alter the ability of the cardiovascular system to react to changes in afterload following anesthesia, but it is well accepted that this ability is compromised.[28,31] Therefore, when modeling the hemodynamics in the catheter models, we assumed that characteristics of the arterial system (e.g., parameters defining the heart and Windkessel models) remained constant despite any changes in afterload introduced by the presence of the catheters. Figure 3

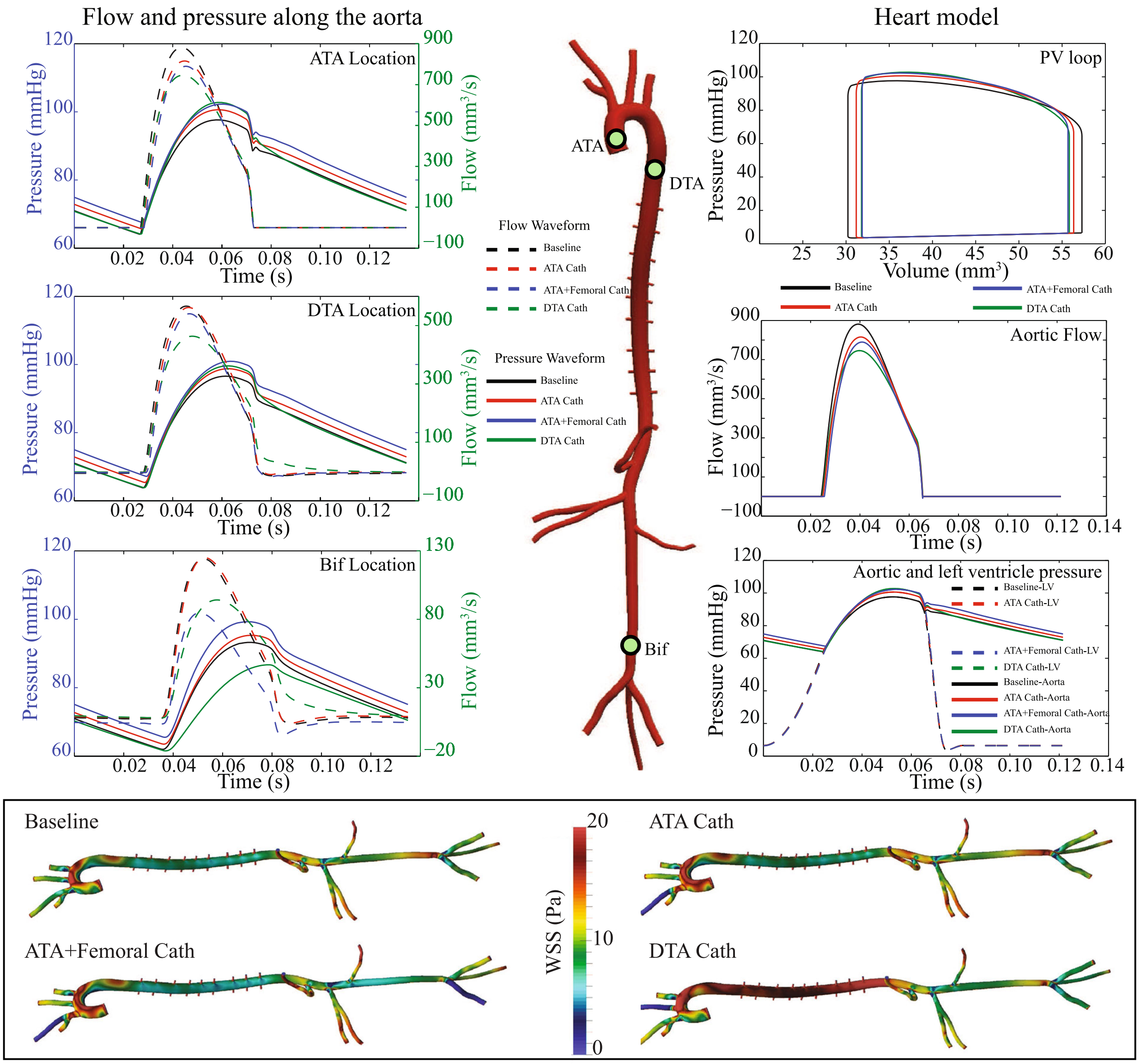

FIGURE 3. Comparison of hemodynamics at three sites (in the ATA, in the DTA, and near the aorto-iliac bifurcation—Bif) in the baseline, ATA Cath, ATA + Femoral Cath, and DTA Cath models.

summarizes the computed hemodynamics for the baseline, ATA Cath, ATA + Femoral Cath, and DTA Cath models. The left side of the figure compares flow (dashed line) and pressure (solid line) at three different locations along the aorta: the ascending thoracic aorta, descending thoracic aorta, and abdominal aorta just proximal to the iliac bifurcation. In particular, we found

Ascending Thoracic Aortic (ATA) Location

Peak and mean flows for the ATA Cath model (cf. Fig. 1d) decreased by 7.4 and 7.1%, respectively, relative to the baseline model. The peak and mean flow decreased further for the ATA + Femoral Cath to 10.4 and 15.3% and for the DTA Cath model to 15.4 and 11.2%, respectively. In terms of pressure, the ATA Cath induced an increase in peak and mean pressure of 3.0 and 2.7% relative to the baseline model; the ATA + Femoral Cath induced an increase in peak and mean pressure of 4.7 and 4.9% relative to the baseline model; the DTA Cath induced a larger increase in peak and mean pressure of 5.2 and 2.3%.

Descending Thoracic Aortic (DTA) Location

The flows in the baseline and ATA Cath models were virtually the same. The peak and mean flows in the ATA + Femoral Cath model were smaller (4.6 and 7.3%) relative to those in the baseline model, and

	Baseline	ATA Cath	ATA+Femoral Cath	DTA Cath
CO (mm^3/s)	200.47	186.29	176.32	178.05
% change	-	-7.1%	-12.1%	-11.2%

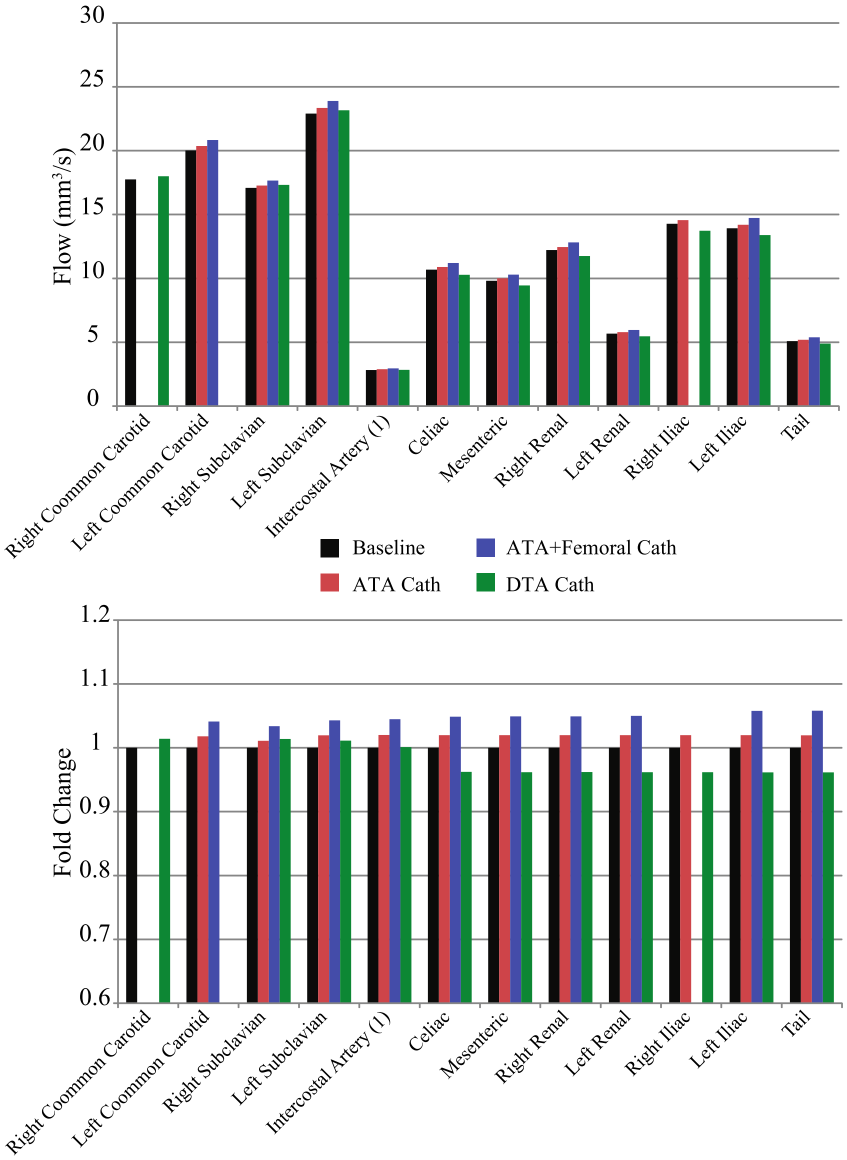

FIGURE 4. Comparison of flow splits for the baseline, ATA Cath, ATA + Femoral Cath, and DTA Cath models. The top plot provides total flows to different branches; the bottom plot shows differential splits as fold change with respect to the baseline model for each catheter model.

even smaller in the DTA Cath model (18.1 and 2.7%). These results were determined by a combination of reduced cardiac output due to higher afterload and diversion of flow to the upper branches due to the presence of the catheter in the descending aorta (Fig. 4). In terms of pressure, the ATA Cath induced an increase in peak and mean pressure of 2.3 and 2.4% relative to the baseline model. The ATA + Femoral Cath induced an increase in peak and mean pressure of 4.6 and 4.9% whereas in the DTA Cath model, the systolic and mean pressures increased by 3.1 and 1.4% relative to the baseline model, respectively.

Aorto-Iliac Bifurcation (Bif) Location

The flows in the baseline and ATA Cath were very similar. Peak and mean flow decreased, relative to the baseline model, for the ATA + Femoral Cath model by 31.8 and 38.0% and for the DTA Cath model by 24.3 and 3.0%, respectively. In terms of pressure, the ATA Cath induced an increase in peak and mean pressure of 2.1 and 2.3%, the ATA + Femoral Cath induced an increase in peak and mean pressure of 6.5 and 6.0%, and in the DTA Cath model, the systolic pressure and mean pressure decreased by 7.0 and 3.4%—all relative to the baseline model, respectively. All pressure traces at this location also revealed a clear phase lag relative to those at the ATA location, a clear sign of altered pulse wave propagation, which expectedly was more noticeable due to the longer distance between the ascending and most distal aortic locations.

The right side of Fig. 3 also compares left ventricular function for the four models by examining the pressure–volume loop, aortic flow, and aortic and left ventricular pressures. Vessel occlusion and catheter insertion resulted in decreased stroke volume and increased left ventricular and ascending aortic pressure compared to the baseline model. These changes were smaller in the ATA Cath compared to the ATA + Femoral Cath and DTA Cath models.

The bottom panel of Fig. 3 shows a comparison between the contours of peak systolic WSS for the different models. As expected, the DTA Cath has a high impact on aortic WSS due to the reduction of luminal area caused by the catheter. Conversely, both the ATA + Femoral Cath and the ATA Cath show similar WSS to the baseline model. Lastly, the occluded vessels at the various catheter insertion points have null WSS.

Figure 4 shows flow splits given as a fraction of total regional flow (top panel) and splits given as fold change with respect to the baseline (bottom panel) for all the models. As expected, the right and left common carotids and femoral arteries show no flow when they were the site of access for the different catheters. There was less flow in the lower vessels for the DTA Cath because of the larger resistance in the distal aorta. The ATA + Femoral Cath case resulted in a larger proportion of flow going to all vessels that remained patent, as expected.

TABLE 7. Aortic pulse wave velocity.

	PWV (m s^{-1}) (centerline length)	PWV (m s^{-1}) (projected length)	% Change
Baseline	4.42	3.52	–
ATA Cath	4.55	3.62	2.86
ATA + Femoral Cath	4.59	3.65	3.85
DTA Cath	4.08	3.25	−7.69

Aortic pulse wave velocity (in m s^{-1}) and % changes relative to the baseline case for the three computational models.

The computations revealed that the different catheters affect PWV in different ways (Table 7). A summary of the results is presented in Fig. 5. Figure 5a shows results of global (aorto-iliac) PWV, whereas Fig. 5b shows regional values of PWV for the different models. Briefly, the aortic-to-iliac PWV increased in the ATA + Femoral Cath model by 3.8% relative to the baseline case (4.59 vs. 4.42 m s^{-1}) due to an overall increase in pressure in the system. Conversely, the DTA Cath model showed a reduction in PWV of 7.7% relative to the baseline (4.08 vs. 4.42 m s^{-1}). These results produced a total difference in the PWV estimate between the two cases of 11.5%, a discrepancy that may be considered significant. Finally, the ATA Cath model results in a modest increase in PWV of 2.9% relative to baseline (4.55 vs. 4.42 m s^{-1}). The bottom part of Fig. 5a compares PWV as measured by the ATA + Femoral Cath and DTA Cath configurations with corresponding values measured in the baseline model. These measurements show discrepancies larger than the above reported aorto-iliac PWV. The ATA + Femoral Cath configuration over-estimated the baseline PWV by 7.29%, whereas the DTA Cath configuration underestimated it by 9.35%. It is important to recall that these two approaches fundamentally measure PWV at different locations. Figure 5b reports local PWV for the baseline and three catheter models. A theoretical justification for the changes in PWV due to the presence of a catheter can be found in the Bramwell and Hill equation, which is derived from the Moens–Korteweg formula through a few substitutions.[2] This relationship $PWV = \sqrt{(VP)/(\rho dV)}$ was applied to a control volume within the thoracic aorta (Fig. 6) for all four simulations. Although local values of PWV were higher (5.10, 5.22, 5.42, 4.70 m s^{-1} for baseline, ATA Cath, ATA + Femoral Cath and DTA Cath cases, respectively) than those for aortic-to-iliac PWV extracted from the simulations (4.42, 4.55, 4.59, 4.08 m s^{-1}), similar trends and values in PWV changes arose. It is important to note that these are PWV values within the aortic control volume rather than the aorto-iliac PWV extracted from the computations. In this analysis, diastolic volumes were used as a reference and differences in volume and pressure (ΔV, ΔP) were obtained between the systolic and diastolic configurations.

DISCUSSION

Animal models offer many advantages in cardiovascular research, including the ability to match *in vivo* and

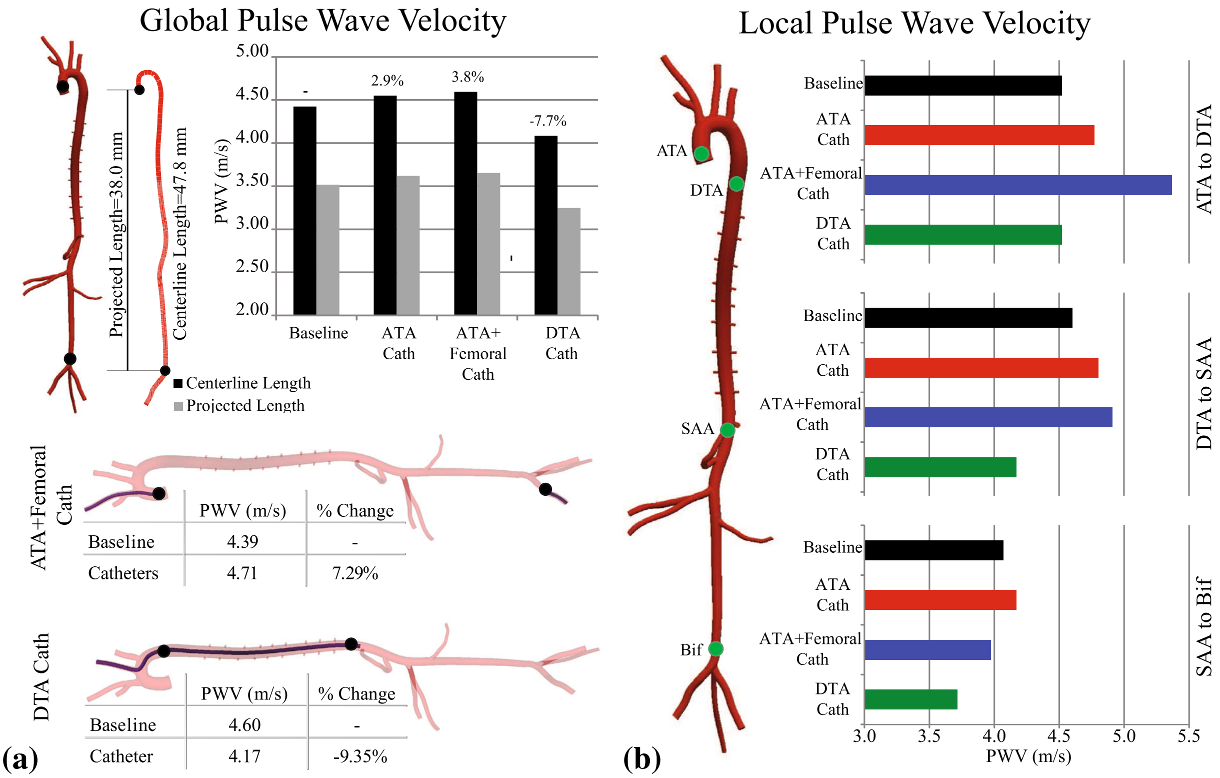

FIGURE 5. (a) Comparison of aorto-iliac PWV in the baseline, ATA Cath, ATA + Femoral Cath, and DTA Cath models, where the percent change is given with respect the baseline model (upper part); comparison of PWV measured by the catheters sensors in each feasible case, compared with the baseline model (bottom part); (b) Comparison of computed local PWV in the baseline, ATA Cath, ATA + Femoral Cath, and DTA Cath models.

in vitro data and to collect longitudinal information. In the case of mice, however, measurements can be complicated by the small size (inner diameter of central arteries ranging between 500 and 1500 μm) and fast heart rate (between 400 and 600 bpm). Central pulse pressure (cPP) and pressure pulse wave velocity (PWV) have become important measurements in humans as well as in animal models. As the most sensitive marker of arterial stiffness, PWV has been measured in mice using a variety of experimental procedures, both invasive and non-invasive. Invasive procedures involve the insertion of a fluid-filled cannula or a catheter within the arterial lumen, hence allowing for measurements of blood pressure. The device diameter is often much smaller than the lumen diameter in humans, but such is not the case in mice because of their small vessels. The inherent risk of such procedures is that the presence of the measuring tool can alter the global hemodynamics and thus affect the physical quantities of interest. Marque *et al.*[23] used chronically implanted polyethylene cannulas having an outer diameter of 1.83F to measure PWV between the descending thoracic aorta and the abdominal aorta in a mouse model of Marfan syndrome. Jung *et al.*[17] instead employed a smaller catheter (diameter of 1.2F) which was introduced through a large portion of the descending aorta and possibly into the abdominal aorta (cf. their Figs. 5a and 1e herein). Finally, Weisbrod *et al.*[33] used the same pressure catheter used in our measurements (diameter of ~1F) and recorded blood pressure waveforms simultaneously from two locations along the aorta (arch and infrarenal abdominal aorta).

Non-invasive procedures instead involve measurements of waveforms associated with the arterial pressure, such as the arterial distensibility and the blood velocity. Hartley *et al.*[13] showed that the upstroke of the blood velocity waveform measured *via* pulsed-wave Doppler in different sections of the aorta (arch and infrarenal abdominal aorta) coincides with the upstroke of the tonometric pressure waveform at the same sites, thus justifying measurements of PWV from the Doppler velocity signal. Currently, Doppler velocimetry represents the most reliable way to measure PWV non-invasively. Yet, the majority of studies in the literature employ commercial ultrasound systems such as the Visualsonic Vevo 770 or 2100 where measurement of the time intervals between the peak of the R-wave and the foot of the blood velocity signals must be performed manually within the commercial data analysis software. Based on our experience, automatic

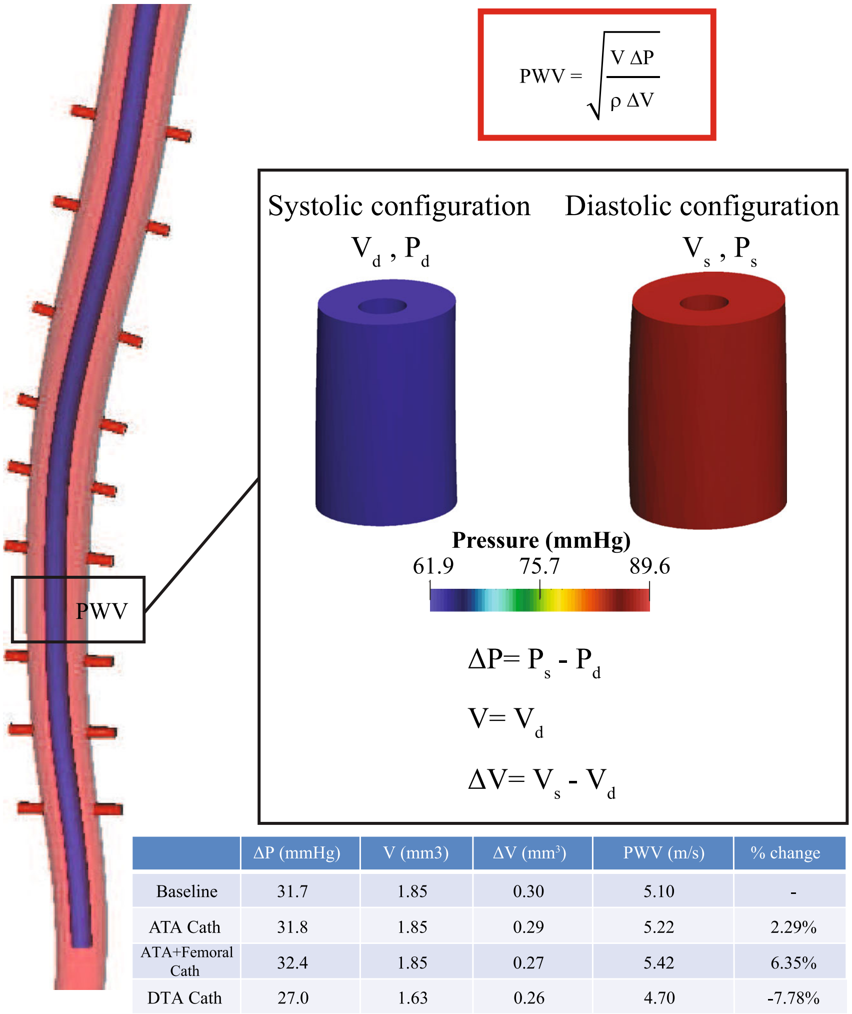

	ΔP (mmHg)	V (mm3)	ΔV (mm^3)	PWV (m/s)	% change
Baseline	31.7	1.85	0.30	5.10	-
ATA Cath	31.8	1.85	0.29	5.22	2.29%
ATA+Femoral Cath	32.4	1.85	0.27	5.42	6.35%
DTA Cath	27.0	1.63	0.26	4.70	-7.78%

FIGURE 6. Control volume for the Bramwell and Hill analysis; volume and pressure are shown in systolic and diastolic configurations.

measurements performed on the recorded waveforms are much more reliable than manual measurements over few cardiac cycles. For this reason, we extracted raw blood velocity waveforms and measured pulse transit times over 25–30 cardiac cycles using a custom Matlab script. Other non-invasive methods to assess PWV in mice include the measurement of local flow and cross-sectional area[34] or applanation tonometric signals.[20] The flow-area method represents only an indirect estimate of local PWV based on a set of assumptions rooted in linear elasticity, while applanation tonometry is much more sensitive to noise and interfering respiratory movements than Doppler velocimetry. Finally, it should be noted that for each of the aforementioned methods, the major source of variability results from measuring the distance between the sites where the proximal and distal waveforms were recorded. Such distances should be evaluated along the centerline of the aortic region of interest, whereas most frequently is approximated by measuring the distance between the probe locations on the skin surface.

Instrumentation or equipment may disturb the characteristics of the system being assessed by perturbing different fields of interest. A tacit assumption is that such perturbations should be negligible in a well-designed experiment. The goals of this work were twofold: to develop a new computational model of murine hemodynamics that includes effects of regional variations in biaxial wall properties and to use this model to evaluate potential sources of error in the invasive evaluation of blood pressure and PWV using commercially available catheters. To this end, four main scenarios were considered: a baseline model represented by a healthy mouse under anesthesia whereas the same overall geometric model and anesthetized conditions were used to model catheters placed within the ascending thoracic aorta and femoral artery or along the descending thoracic aorta. Our computational approach thus allowed us to assess roles of the catheter alone, independent of possible variations in experimental conditions as would be present in experimental assessments.

We were able to reproduce physiological pressure waveforms, flow distributions, and values of PWV using the following methods: a multi-domain method that couples a heart model with the ascending aorta and Windkessel models for all major vascular outlets in the 3D vascular model, a coupled-momentum method for FSI that included regional variations in anisotropy and wall stiffness, an external tissue boundary condition to represent perivascular support, and a method for a posteriori gradient-based mesh adaptation. This is the first time that this combination of methods has been achieved in the mouse vasculature, which was necessary to realistically capture all of the available experimental hemodynamic data. In contrast, most prior computational fluid dynamics models for mice employ the rigid wall assumption and/or simplified geometries (e.g.,[4,15,30]), which disallow (or sometimes entirely preclude) accurate calculations of blood pressure and PWV despite possibly achieving good estimates of the velocity field.

Using a coupled heart model, rather than imposing flow or pressure as an inlet boundary condition, was of particular importance herein for it allowed us to investigate changes in cardiac output among all the different cases and, more importantly, to obtain more reliable results. The larger the volume occupied by the catheter within the vasculature, the greater the resistance that the heart has to work against, and thus the lower the cardiac output. Assuming that the cardiovascular system is not able to adjust to a changing afterload under anesthesia, parameters tuned for the baseline model were fixed for each catheter simulation. That is, we assumed that following the initial vasodilatation or vasoconstriction induced by the anesthesia, the heart, arteries, arterioles, and capillaries would lose most of their ability to adapt acutely. Such an assumption needs to be evaluated experimentally.

Placement of the catheter in the DTA Cath caused, relative to the baseline model, a decrease in cardiac output, a decrease in flow to the distal branches, and a lower PWV. All of these outcomes appear to have been due primarily to the volume occupied by the catheter, which effectively represented a large resistance that reduced cardiac output and diverted more flow to the upper branches where the resistance was smaller. Larger catheters than used in our simulations can be found in literature (e.g.,[21,25]), and therefore probably have even greater effects on the hemodynamics. Conversely, we found that the combination of catheters in the ATA + Femoral Cath case resulted in similar drop in cardiac output, and an increase in PWV due to an overall increase in pressure in the system. Finally, it is important to note that the calculation of PWV is very sensitive to the distance between locations where the pressure is measured. Figure 5 compares values of PWV when computed with the actual length travelled by the pressure wave between measurement sites (''centerline length'', 47.8 mm in the case considered here) and with the ''projected length'' between measurement sites (38.0 mm in this case). This ''projected length'' is what is utilized in most experiments, and it may significantly under-estimate the reported values of PWV: the difference was 21% for the example considered here, but this difference may be much larger for mice with more tortuous aortas.

Limitations

The baseline murine hemodynamics presented in this paper correspond to a single illustrative case, where different measurements were taken in different animals. We did not assess potential differences in errors across multiple mice, including those of different ages (and hence body mass), genotypes, or sex. Given the limited sizes of the commercially available catheters, it is likely that the degree of the errors will vary from mouse to mouse and similar simulations would be useful depending on the groups of mice to be studied. Indeed, there is variability even within the same age, sex, and genotype and variability in heart rate and blood pressure depending on the anesthetic used. Ultimately, a careful comparison across all possible variations would be useful, to include an uncertainty quantification given the spatial and temporal resolutions available for measuring the requisite geometries, properties, and applied loads needed for formulate the initial-boundary value problem.

In our work cardiac output and central pressure were not measured in the same animal. However, the value of cardiac output is coherent with the combination of blood velocity and diameter of the vessel measured in the ascending thoracic aorta with Ultrasound.

Lastly, in our FSI method, the edges of each outlet surface as well as the inlet surface are fixed in space; the latter does not allow the motion of the heart or its effects on the extension of the ascending aorta to be captured. Although future models should include this complexity, we do not expect that this limitation has an important impact on the computed PWV, which is mainly determined by the geometry of the aorta and the arterial stiffness.

CONCLUSION

The present results suggest that two catheter systems commonly used to assess PWV in mice perturb the hemodynamics in different ways: even though the reduction in cardiac output is similar, the dual catheter approach (ATA + Femoral Cath) increases PWV by increasing pressure in the system due to the higher peripheral vascular resistance offered by two completely occluded vessels. Conversely, the dual sensor, single catheter approach (DTA Cath) decreases the PWV by decreasing the pressure in the system due to higher viscous loses in the aorta. Furthermore, it is important to note that these two systems fundamentally measure PWV at two different locations, thus different values would be obtained even if the hemodynamic disturbances were negligible.

Whereas the present results reveal general considerations when using catheter-based methods to measure PWV, we note that the extents of these effects will likely be different in smaller vs. larger mice, younger vs. older mice, and wild-type vs. mutant mice. A complete evaluation should address the specific mice to be used.

ACKNOWLEDGMENTS

This work was supported, in part, by a Grant from the NIH (R01 HL105297), by the European Research Council Grant Agreement No. 307532, and by the United Kingdom Department of Health *via* the National Institute for Health Research (NIHR) comprehensive Biomedical Research Centre award to Guy's & St Thomas' NHS Foundation Trust in partnership with King's College London and King's College Hospital NHS Foundation Trust. The authors acknowledge Simmetrix, Inc. (http://www.simmetrix.com/) for their MeshSim mesh generation library. Lastly, the authors gratefully thank Dr Z. Zhuang who executed micro-CT imaging on the vascular corrosion cast, M.R. Bersi who segmented the acquired volume, Dr. K.D. Lau who provided support with tuning of the heart model, and Dr. N. Xiao who developed the algorithm for spatial interpolation of tissue stiffness.

CONFLICT OF INTEREST

The authors declare that they do not have any conflicts of interest related to this work.

REFERENCES

[1] Baek, S., R. L. Gleason, K. R. Rajagopal, and J. D. Humphrey. Theory of small on large: potential utility in computations of fluid–solid interactions in arteries. *Comput. Methods Appl. Mech. Eng.* 196:3070–3078, 2007.

[2] Bramwell, J. C., and A. V. Hill. The velocity of the pulse wave in man. *Proc. R. Soc. Lond. B Biol. Sci.* 93:298–306, 1922.

[3] Claeys, M. A., E. Gepts, and F. Camu. Haemodynamic changes during anaesthesia induced and maintained with propofol. *Br. J. Anaesth.* 60:3–9, 1988.

[4] Feintuch, A., P. Ruengsakulrach, A. Lin, J. Zhang, Y.-Q. Zhou, J. Bishop, L. Davidson, D. Courtman, F. S. Foster, D. A. Steinman, R. M. Henkelman, and C. R. Ethier. Hemodynamics in the mouse aortic arch as assessed by MRI, ultrasound, and numerical modeling. *Am. J. Physiol. Heart Circ. Physiol.* 292:H884–H892, 2007.

[5] Ferruzzi, J., M. R. Bersi, S. Uman, H. Yanagisawa, and J. D. Humphrey. Decreased elastic energy storage, not increased material stiffness, characterizes central artery dysfunction in fibulin-5 deficiency independent of sex. *J. Biomech. Eng.* 2015. doi:10.1115/1.4029431.

[6] Ferruzzi, J., D. A. Vorp, and J. D. Humphrey. On constitutive descriptors of the biaxial mechanical behaviour of human abdominal aorta and aneurysms. *J. R. Soc. Interface* 8:435–450, 2011.

[7] Figueroa, C. A., S. Baek, C. A. Taylor, and J. D. Humphrey. A computational framework for fluid–solid-growth modeling in cardiovascular simulations. *Comput. Methods Appl. Mech. Eng.* 198:3583–3602, 2009.

[8] Figueroa, C. A., I. E. Vignon-Clementel, K. E. Jansen, T. J. R. Hughes, and C. A. Taylor. A coupled momentum method for modeling blood flow in three-dimensional deformable arteries. *Comput. Methods Appl. Mech. Eng.* 195:5685–5706, 2006.

[9] Gaddum, N. R., J. Alastruey, P. Beerbaum, P. Chowienczyk, and T. Schaeffter. A technical assessment of pulse wave velocity algorithms applied to non-invasive arterial waveforms. *Ann. Biomed. Eng.* 41:2617–2629, 2013.

[10] Greve, J. M., A. S. Les, B. T. Tang, M. T. Draney Blomme, N. M. Wilson, R. L. Dalman, N. J. Pelc, and C. A. Taylor. Allometric scaling of wall shear stress from mice to humans: quantification using cine phase-contrast MRI and computational fluid dynamics. *Am. J. Physiol. Heart Circ. Physiol.* 291:H1700–H1708, 2006.

[11] Guo, X., Y. Kono, R. Mattrey, and G. S. Kassab. Morphometry and strain distribution of the C57BL/6 mouse aorta. *Am. J. Physiol. Heart Circ. Physiol.* 283:H1829–H1837, 2002.

[12] Hartley, C., A. Reddy, S. Madala, B. Martin-McNulty, R. Vergona, M. E. Sullivan, M. Halks-Miller, G. E. Taffet, L. H. Michael, M. L. Entman, and Y.-X. Wang. Hemodynamic changes in apolipoprotein E-knockout mice. *Am. J. Physiol. Heart Circ. Physiol.* 279:H2326–H2334, 2000.

[13] Hartley, C. J., G. E. Taffet, L. H. Michael, T. T. Pham, and M. L. Entman. Noninvasive determination of pulse-wave velocity in mice. *Am. J. Physiol. Heart Circ. Physiol.* 273:H494–H500, 1997.

[14] Hartley, C. J., G. E. Taffet, A. K. Reddy, M. L. Entman, and L. H. Michael. Noninvasive cardiovascular phenotyping in mice. *ILAR J.* 43:147–158, 2002.

[15] Huo, Y., X. Guo, and G. S. Kassab. The flow field along the entire length of mouse aorta and primary branches. *Ann. Biomed. Eng.* 36:685–699, 2008.

[16] Janssen, B. J. A., T. De Celle, J. J. M. Debets, A. E. Brouns, M. F. Callahan, and T. L. Smith. Effects of anesthetics on systemic hemodynamics in mice. *Am. J. Physiol. Heart Circ. Physiol.* 287:H1618–H1624, 2004.

[17] Jung, S., S. Jandu, and J. Steppan. Increased tissue transglutaminase activity contributes to central vascular stiffness in eNOS knockout mice. *Am. J. Physiol. Hear. Circ. Physiol.* 305:H803–H810, 2013.

[18] Kim, H. J., I. E. Vignon-Clementel, C. A. Figueroa, J. F. LaDisa, K. E. Jansen, J. A. Feinstein, and C. A. Taylor. On coupling a lumped parameter heart model and a three-dimensional finite element aorta model. *Ann. Biomed. Eng.* 37:2153–2169, 2009.

[19] Lau, K. D., and C. A. Figueroa. Simulation of short-term pressure regulation during the tilt test in a coupled 3D-0D closed-loop model of the circulation. *Biomech. Model. Mechanobiol.* 2015. doi:10.1007/s10237-014-0645-x.

[20] Leloup, A. J. A., P. Fransen, C. E. Van Hove, M. Demolder, G. W. De Keulenaer, and D. M. Schrijvers. Applanation tonometry in mice: a novel noninvasive technique to assess pulse wave velocity and arterial stiffness. *Hypertension* 64:195–200, 2014.

[21] Li, Y., G. Takemura, H. Okada, S. Miyata, M. Esaki, R. Maruyama, H. Kanamori, L. Li, A. Ogino, Y. Misao, N. C. Khai, A. Mikami, S. Minatoguchi, T. Fujiwara, and H. Fujiwara. Treatment with granulocyte colony-stimulating factor ameliorates chronic heart failure. *Lab. Invest.* 86:32–44, 2006.

[22] Lujan, H. L., and S. E. DiCarlo. Cardiac output, at rest and during exercise, before and during myocardial ischemia, reperfusion, and infarction in conscious mice. *Am. J. Physiol. Regul. Integr. Comp. Physiol.* 304:R286–R295, 2013.

[23] Marque, V., H. Van Essen, H. A. J. Struijker-Boudier, J. Atkinson, and I. Lartaud-Idjouadiene. Determination of aortic elastic modulus by pulse wave velocity and wall tracking in a rat model of aortic stiffness. *J. Vasc. Res.* 38:546–550, 2001.

[24] Moireau, P., N. Xiao, M. Astorino, C. A. Figueroa, D. Chapelle, C. A. Taylor, and J.-F. Gerbeau. External tissue support and fluid-structure simulation in blood flows. *Biomech. Model. Mechanobiol.* 11:1–18, 2012.

[25] Okada, H., G. Takemura, K. Kosai, Y. Li, T. Takahashi, M. Esaki, K. Yuge, S. Miyata, R. Maruyama, A. Mikami, S. Minatoguchi, T. Fujiwara, and H. Fujiwara. Postinfarction gene therapy against transforming growth factor-beta signal modulates infarct tissue dynamics and attenuates left ventricular remodeling and heart failure. *Circulation* 111:2430–2437, 2005.

[26] Sahni, O., J. Müller, K. E. Jansen, M. S. Shephard, and C. A. Taylor. Efficient anisotropic adaptive discretization of the cardiovascular system. *Comput. Methods Appl. Mech. Eng.* 195:5634–5655, 2006.

[27] Schmeling, W., and N. Farber. Anesthetic actions on cardiovascular control mechanisms in the central nervous system. *Adv. Pharmacol.* 31:617–642, 1994.

[28] Shimokawa, A., T. Kunitake, M. Takasaki, and H. Kannan. Differential effects of anesthetics on sympathetic nerve activity and arterial baroreceptor reflex in chronically instrumented rats. *J. Auton. Nerv. Syst.* 72:46–54, 1998.

[29] Shroff, S., J. Janicki, and K. Weber. Evidence and quantitation of left ventricular systolic resistance. *Am. J. Physiol. Heart Circ. Physiol.* 249:H358–H370, 1985.

[30] Trachet, B., M. Renard, G. De Santis, S. Staelens, J. De Backer, L. Antiga, B. Loeys, and P. Segers. An integrated framework to quantitatively link mouse-specific hemodynamics to aneurysm formation in angiotensin II-infused ApoE −/− mice. *Ann. Biomed. Eng.* 39:2430–2444, 2011.

[31] Usselman, C., L. Mattar, J. Twynstra, I. Welch, and J. Shoemaker. Rodent cardiovascular responses to baroreceptor unloading: effect of plane of anaesthesia. *Appl. Physiol. Nutr. Metab.* 36:376–381, 2011.

[32] Vignon-Clementel, I. E., C. A. Figueroa, K. E. Jansen, and C. A. Taylor. Outflow boundary conditions for 3D simulations of non-periodic blood flow and pressure fields in deformable arteries. *Comput. Methods Biomech. Biomed. Eng.* 13:1–16, 2010.

[33] Weisbrod, R., T. Shiang, L. Al Sayah, J. L. Fry, S. Bajpai, C. A. Reinhart-King, H. E. Lob, L. Santhanam, G. Mitchell, R. A. Coen, and F. Seta. Arterial stiffening precedes systolic hypertension in diet-induced obesity. *Hypertension* 62:1105–1110, 2013.

[34] Williams, R., A. Needles, E. Cherin, Y.-Q. Zhou, R. M. Henkelman, S. L. Adamson, and F. S. Foster. Noninvasive ultrasonic measurement of regional and local pulse-wave velocity in mice. *Ultrasound Med. Biol.* 33:1368–1375, 2007.

[35] Xiao, N., J. Alastruey, and C. A. Figueroa. A systematic comparison between 1-D and 3-D hemodynamics in compliant arterial models. *Int. J. Numer. Methods Biomed. Eng.* 30:204–231, 2013.

[36] Xiao, N., J. D. Humphrey, and C. A. Figueroa. Multi-scale computational model of three-dimensional hemodynamics within a deformable full-body arterial network. *J. Comput. Phys.* 244:22–40, 2014.